Small Methods

small methods
www.small-methods.com

RESEARCH ARTICLE

A Defect-Engineered Vacuum Evaporation Strategy for High-Efficiency Indoor Perovskite Mini Solar Modules

Shih-Han Huang[1] | Ssu-Yung Chung[1] | Fang-Chun Su[2] | Chia-Feng Li[1,3] | You-Ren Chen[1,4] | Ting-Han Lin[5] | Hou-Chin Cha[1,6] | Yi-Sheng Chen[1,6] | Chih-Chien Lee[2] | Yu-Ching Huang[1,4,5,7] | Shun-Wei Liu[1,5,6,8]

[1]Organic Electronics Research Center, Ming Chi University of Technology, New Taipei City, Taiwan | [2]Department of Electronic Engineering, National Taiwan University of Science and Technology, Taipei City, Taiwan | [3]Department of Materials Science and Engineering, National Taiwan University, Taipei, Taiwan | [4]Department of Materials Engineering, Ming Chi University of Technology, New Taipei City, Taiwan | [5]Center For Sustainability and Energy Technologies, Chang Gung University, Taoyuan, Taiwan | [6]College of Engineering, Ming Chi University of Technology, New Taipei City, Taiwan | [7]Research Center for Critical Issues, Academia Sinica, Taipei, Taiwan | [8]Department of Electronic Engineering, Ming Chi University of Technology, New Taipei City, Taiwan

Correspondence: Yu-Ching Huang (huangyc@mail.mcut.edu.tw) | Shun-Wei Liu (swliu@mail.mcut.edu.tw)

Received: 22 December 2025 | **Revised:** 9 March 2026 | **Accepted:** 31 March 2026

Keywords: defect passivation | fully evaporated | indoor | perovskite

ABSTRACT

Fully vacuum-evaporated perovskite solar cells (PSCs) offer a solvent-free, scalable platform for indoor photovoltaics, yet performance is often limited by incomplete phase conversion and high defect densities. Here, we report a sequential vacuum-evaporation strategy that enables the formation of high-quality perovskite absorbers specifically optimized for low-intensity indoor light harvesting. By co-evaporating PbI_2 with a controlled fraction of $PbCl_2$, the dense stacking characteristic of thermally deposited PbI_2 is effectively disrupted, promoting homogeneous organic–inorganic interdiffusion and near-complete perovskite phase conversion. Additionally, a thin CsI interlayer introduced prior to thermal annealing stabilizes the photoactive phase and suppresses defect formation at both the bulk and interfacial levels. Consequently, the optimized fully evaporated PSCs deliver record indoor power conversion efficiencies of 41.60% at 900 lux and 41.22% at 300 lux under TL84 illumination. Transient photovoltage and photocurrent analyses reveal prolonged carrier lifetimes and accelerated charge extraction, indicative of substantially reduced nonradiative recombination. Importantly, the devices exhibit markedly enhanced operational stability and enable a perovskite mini module (3.9 cm^2), achieving over 38% efficiency at 900 lux under indoor lighting. Collectively, this work establishes a practical and industrially compatible pathway toward high-performance, scalable, fully evaporated perovskite photovoltaics, advancing their deployment in next-generation self-powered indoor electronic systems.

1 | Introduction

The rapid development of Internet of Things (IoT) devices, driven by advancements in fifth-generation (5G) communication and wireless sensing technologies [1, 2]. IoT has led to an exponential increase in the number of autonomous sensor nodes deployed in smart homes, industrial monitoring, environmental tracking, and logistics management. Until now, the widespread adoption of IoT devices has been hindered by reliance on conventional batteries, which introduce issues such as large maintenance demand, limited lifetime, bulky form factor, and environmental concerns associated with chemical waste [3, 4]. As IoT ecosystems continue to scale toward billions of interconnected devices, powering them sustainably becomes a critical challenge. To overcome this bottleneck, self-powered IoT systems capable of harvesting ambient environmental energy have emerged as a promising pathway to enable long-term, maintenance-free operation [5]. Among various self-powered approaches, ambient light harvesting using

photovoltaic (PV) cells has gained significant attention because indoor illumination (typically 0.01–10 mW cm^{-2}) is consistently available in most IoT environments [6]. Photovoltaic-powered sensors can thus operate continuously by converting weak indoor light or diffuse low-intensity solar irradiation into electrical energy for sensing, processing, and wireless transmission. While crystalline-silicon solar cells dominate outdoor PV markets, their performance under low-light conditions deteriorates significantly because of their low absorption coefficient and increased parasitic losses, making them less suitable for indoor energy harvesting [7, 8].

In recent years, several emerging photovoltaic technologies have been explored for indoor energy harvesting, including amorphous silicon, organic photovoltaics, colloidal quantum dots, perovskite solar cells (PSCs), and dye-sensitized solar cells [9–13]. Among these, PSCs have quickly become the most commercially promising candidate for indoor energy harvesting due to their high absorption coefficient, excellent defect tolerance, tunable bandgap, and strong compatibility with low-cost and scalable manufacturing. Remarkably, indoor PSCs have achieved power conversion efficiency (PCE) exceeding 40% under 1000 lux of light-emitting diode (LED) illumination, outperforming all other PV technologies. [14] Although most high-efficiency PSCs are fabricated using one-step solution-based coating processes, vacuum-based thermal evaporation offers several key advantages for large-scale production, including solvent-free deposition, superior film uniformity, precise stoichiometric control, high reproducibility, and strong compatibility with existing industrial manufacturing infrastructure [15, 16]. These advantages make fully evaporated PSCs architectures particularly attractive for high-throughput manufacturing of ambient-light photovoltaic modules. Several vacuum-based deposition strategies have been reported, such as single-source evaporation [17–19], sequential evaporation [20–22], and co-evaporation [23, 24]. Co-evaporation provides exceptional film uniformity and phase control, but using multiple precursors (e.g., Formamidinium iodide, PbI_2, Cs salts) presents practical challenges due to differing vapor pressures and rate-control requirements. Sequential evaporation is expected to mitigate these issues; however, despite the technological potential, only one publication reports an indoor PSC fabricated entirely by vacuum evaporation, achieving 30.25% under 1000 lx LED illumination [25]. This lack highlights how underdeveloped fully-evaporated indoor PSCs currently are.

Currently, the widely studied high-efficiency PSCs for outdoor applications primarily concentrate on perovskite compositions with a bandgap of 1.5–1.6 eV. Despite rapid progress, indoor PSCs face different challenges from outdoor photovoltaics because the illumination spectrum and intensity differ drastically between sunlight and indoor LEDs [26–28]. Under low-photon-flux conditions, carrier generation, recombination pathways, and interfacial mechanisms fundamentally change. Recent studies demonstrated that factors such as perovskite thickness, defect density, and interfacial recombination play a significantly amplified role under indoor light [29–31]. In particular, defect-induced nonradiative recombination becomes more detrimental at low light, where intrinsic carrier concentrations are limited and trap-assisted recombination dominates. These studies collectively highlight the influence of light sources and key factors affecting solar cell performance under different light intensities. Moreover, many reported indoor PSCs achieve >40% PCE at 1000 lx but experience a significant performance drop below 500 lx, indicating that conventional passivation strategies optimized for 1-sun performance are insufficient for low-intensity environments [27, 32]. These results highlight the urgency of developing defect-suppression and interface-engineering strategies specifically tailored for indoor photovoltaics.

In this work, we address these challenges by developing a vacuum-evaporated sequential deposition method to fabricate high-quality perovskite active layers suitable for indoor photovoltaics. By precisely tuning the lead-halide ratio during the initial vapor-deposited layer, we facilitate complete perovskite phase conversion during the subsequent FAI reaction. Furthermore, controlled incorporation of CsI before the phase transition effectively suppresses interfacial defects and mitigates nonradiative recombination losses, which is factors that are especially detrimental under indoor light. As a result, the defect-passivated, fully-evaporated PSCs achieve outstanding indoor PCEs of 41.60% at 900 lx TL84 (263.63 μW cm^{-2}) and 41.22% at 300 lx TL84 (90.45 μW cm^{-2}). Furthermore, a large-area perovskite module with an active area of 3.9 cm^2 achieves a PCE exceeding 38% under 900 lx TL84 illumination. These results represent, to the best of our knowledge, the highest reported performances for fully evaporated indoor PSCs to date.

2 | Results and Discussion

For the sequential deposition of inorganic and organic hybrid perovskites, the inorganic compound and organic components can be deposited separately to form evaporated thin films. For the inorganic layers prepared by thermal evaporation, many studies report that the resulting PbI_2 films exhibit a highly dense morphology. This density often hinders the penetration of organic precursors into the PbI_2 layer, thereby limiting the complete conversion of the perovskite phase [33–35]. To disrupt the ordered stacking of PbI_2, the introduction of a hetero-source such as $PbCl_2$ can be effective. Owing to the smaller ionic radius of chloride ions compared to iodide ions, the incorporation of $PbCl_2$ disturbs the regular stacking of PbI_2 lattice. Accordingly, $PbCl_2$ was co-evaporated with PbI_2 during the inorganic layer deposition. The deposition conditions were defined by a fixed PbI_2 deposition rate of 3 Å s^{-1}, accompanied by $PbCl_2$ rates of 0, 0.25, 0.5, and 0.75 Å s^{-1}, denoted as pure PbI_2, low-Cl, medium-Cl, and high-Cl conditions, respectively. Figure 1a represents top-view scanning electron microscopy (SEM) images of PbI_2 film with and without $PbCl_2$ incorporation. The pristine PbI_2 film exhibits a compact morphology with small, needle-like crystallites. Upon incorporation of $PbCl_2$ at deposition rates of 0.25 and 0.5 Å s^{-1}, the needle-like crystal features become more obvious and distinguishable. When the $PbCl_2$ deposition rate increased to 0.75 Å s^{-1}, the film morphology transforms into a distinctive petal-like structure. This observation suggests that the $PbCl_2$ becomes dominant in the mixed PbI_2-$PbCl_2$ crystal stacking at high chlorine content. Figure 1b shows the element composition of iodine and chlorine ratio by the energy-dispersive X-ray spectroscopy (EDS). The pristine PbI_2 film contains only iodine, while the low-Cl and medium-Cl films exhibit I/Cl ratios of 89:11 and 78:22, respectively. In contrast, the high-Cl sample with petal-like morphology represents an I/Cl ratio of 63:37. This indicates

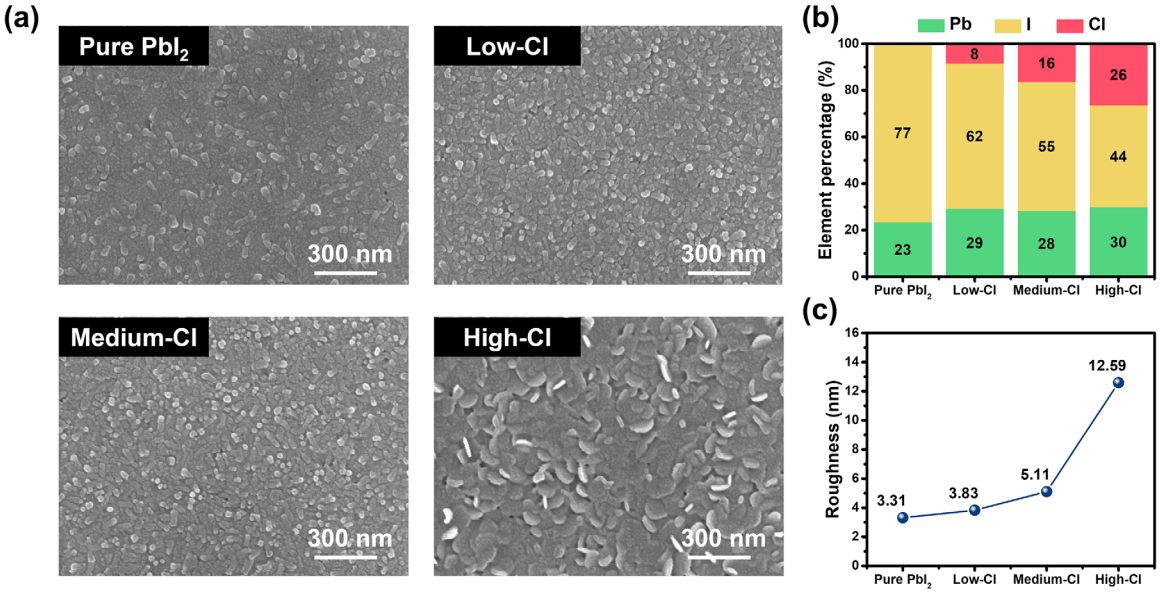

FIGURE 1 | (a) Top-view SEM images of thermally evaporated PbI_2 films with different $PbCl_2$ co-evaporation rates: pure PbI_2, low-Cl, medium-Cl, and high-Cl. (b) I and Cl compositions measured by EDS. (c) Surface roughness of PbI_2 films with increasing $PbCl_2$ content, extracted from AFM measurements.

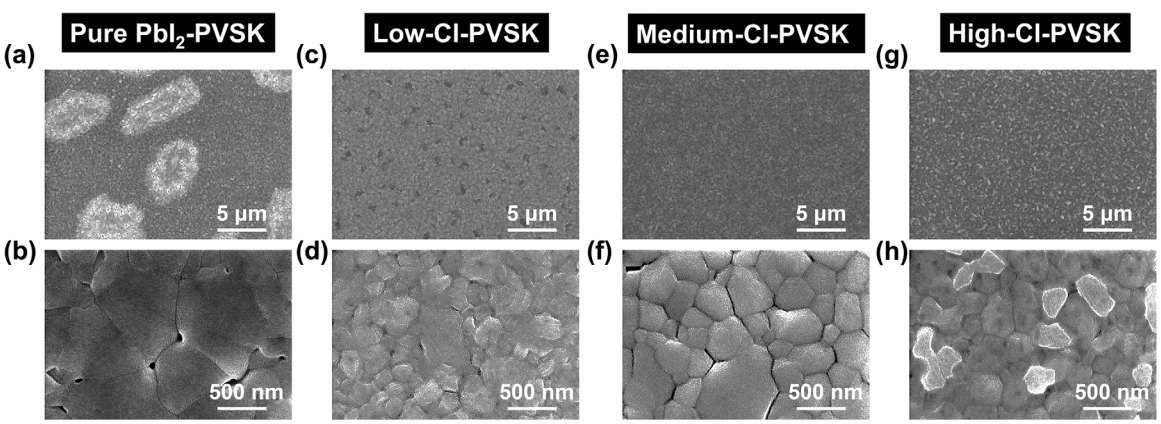

FIGURE 2 | Top-view SEM images of perovskite films derived from inorganic precursor layers with different $PbCl_2$ contents: (a,b) pure PbI_2-based perovskite, (c,d) low-Cl perovskite, (e,f) medium-Cl perovskite, and (g,h) high-Cl perovskite. Low- and high-magnification images are shown in the top and bottom rows, respectively.

that a chlorine content of approximately 37% significantly alters the crystal growth behavior of the inorganic layer. Atomic force microscopy (AFM) images and the corresponding surface roughness values (Figure S1, Figure 1c) reveal that surface roughness increases with increasing $PbCl_2$ content. This trend confirms that the incorporation of hetero $PbCl_2$ effectively disrupts the dense stacking of PbI_2 layer. The transformation changes the originally compact surface into a roughened morphology, which facilitates the vapor-phase diffusion of organic precursors and promotes complete perovskite phase conversion

We hypothesized that an increased surface roughness of the inorganic precursor film would facilitate the diffusion of organic species. This improved diffusion is expected to promote a more complete solid-state reaction and perovskite phase conversion. To evaluate this hypothesis, SEM was employed to examine perovskite films fabricated from inorganic layers with different $PbCl_2$ incorporation ratios, as shown in Figure 2. SEM images were collected at magnifications of 5000×, 25000×, and 50000× for each condition. For perovskite films derived from pristine PbI_2, the morphology at 5000× magnification exhibits randomly distributed bright regions. High-magnification SEM images reveal distinct morphological heterogeneity at the domain boundaries. In these regions, dense areas of fine crystallites coexist with adjacent areas of larger grains and voids, indicating nonuniform phase conversion. In the low-Cl condition, the resulting perovskite film still exhibits small domain distributions. However, high-magnification SEM images reveal a relatively compact surface within individual domains. In contrast, the medium-Cl film shows a uniform and continuous surface already at 5000× magnification, and the compact crystal arrangement is maintained even at higher magnifications. Although the

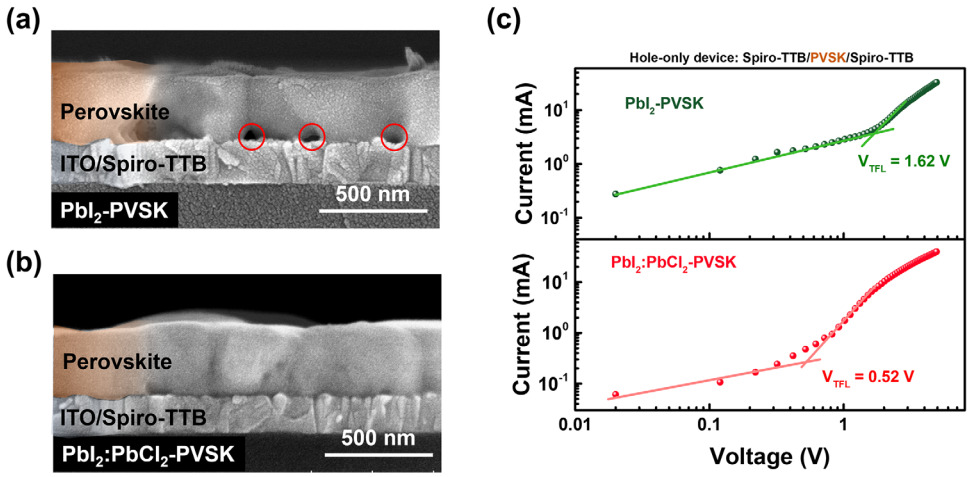

FIGURE 3 | Cross-sectional SEM images of perovskite films prepared from (a) PbI_2 and (b) PbI_2:$PbCl_2$ inorganic precursors. (c) SCLC characteristics of hole-only devices based on the corresponding perovskite films.

high-Cl film exhibits a generally uniform morphology, localized bright agglomerates are observed at smaller length scales. The EDS analysis in Figure S2 shows that these regions have a lower nitrogen (N) ratio than the surrounding crystals. This observation suggests that excessive $PbCl_2$ incorporation introduces competition during the ion-exchange process with PbI_2 during the perovskite phase transition, leading to compositional inhomogeneity. Figure S3 presents the EDS analysis of elemental ratios for perovskite films prepared from different Cl-containing inorganic precursor films. For all conditions, the chloride content in the final perovskite films decreases to nearly negligible levels. This observation suggests that Cl^- ions are initially introduced to disrupt the stacking of PbI_2; however, during the annealing process, they are gradually substituted by I^- ions and subsequently removed as volatile species [36, 37]. When the $PbCl_2$ content becomes excessive, the crystallization of the perovskite phase is perturbed, leading to incomplete or nonuniform phase transformation. Consequently, the incorporation of too much $PbCl_2$ results in morphological degradation of the perovskite films. Based on these structural and morphological analyses, the deposition condition with a PbI_2/$PbCl_2$ rate of 3/0.5 Å s^{-1} is identified as the optimal composition for achieving uniform and high-quality perovskite films.

Cross-section SEM was employed to investigate the vertical morphology of perovskite films, as shown in Figure 3a. The perovskite film fabricated from the pristine PbI_2 film exhibits a large number of voids near the bottom interface, indicating incomplete perovskite conversion. By contrast, incorporation of $PbCl_2$ into the PbI_2 film results in a perovskite film with a dense and uniform morphology at the hole-transporting layer/perovskite interface. The improved vertical homogeneity indicates a more complete phase conversion throughout the absorber layer, which is attributed to the disrupted inorganic precursor packing induced by $PbCl_2$ incorporation. Figure 3b presents the space-charge-limited current (SCLC) measurements used to quantify the bulk defect density of perovskite films prepared from different inorganic precursors. The defect density was extracted using the standard SCLC model and fitting procedure reported in previous studies [38]. The perovskite film derived from pristine PbI_2 exhibits a higher bulk defect density of 9.16×10^{16} cm^{-3}. In comparison, incorporation of $PbCl_2$ significantly reduces the defect density to 2.94×10^{16} cm^{-3}, confirming that improved and complete perovskite phase conversion plays a crucial role in suppressing defect formation within the perovskite layer.

Compared with outdoor sunlight, indoor light sources such as fluorescent lamps and light-emitting diodes (LEDs) emit predominantly within the visible region (400–700 nm) with intensities nearly three orders of magnitude lower than 1-sun conditions [39]. At these low intensities, photovoltaic devices are highly sensitive to losses from Shockley–Read–Hall (SRH) trap-assisted recombination. The low photon flux generates fewer charge carriers, leaving many defect states unoccupied and active as recombination centers, especially at interfaces [40, 41]. Effective defect suppression is the key to achieving high-efficiency indoor perovskite solar cells. Besides controlling defects, phase stability is also critical. In FA-based perovskites, the photoactive α-phase is metastable and tends to transform into the non-photoactive δ-phase during prolonged storage, driven by the unfavorable tolerance factor associated with the large FA^+ cation. This phase instability not only degrades light absorption but also introduces additional structural defects that further exacerbate nonradiative recombination under low-intensity illumination. Here, CsI was incorporated by depositing a CsI interlayer on top of the PbI_2:$PbCl_2$/FAI precursor stack prior to thermal annealing, as illustrated in Figure 4a. Figure 4b presents the absorption spectra of perovskite films with varying CsI thicknesses. After annealing, the initially stacked precursor layers interdiffusion and convert into the perovskite phase. The pristine film exhibits a bandgap of 1.51 eV, consistent with α-$FAPbI_3$. Increasing the CsI thickness to 10, 20, and 30 nm results in gradual bandgap widening to 1.52, 1.53, and 1.53 eV, respectively, indicating successful incorporation of Cs into the perovskite lattice. Top-view SEM images (Figure 4c) were used to examine the surface morphology evolution. The pristine and CsI-modified films with 10 and 20 nm CsI exhibit similar compact and uniform surfaces. In contrast, the film incorporating 30 nm CsI displays noticeable surface precipitates, indicating the onset of phase separation induced by excessive Cs incorporation during thermal annealing. As shown in Figure S4, distinct regions with different crystal morphologies are clearly observed. Elemental analysis indicates that the bright,

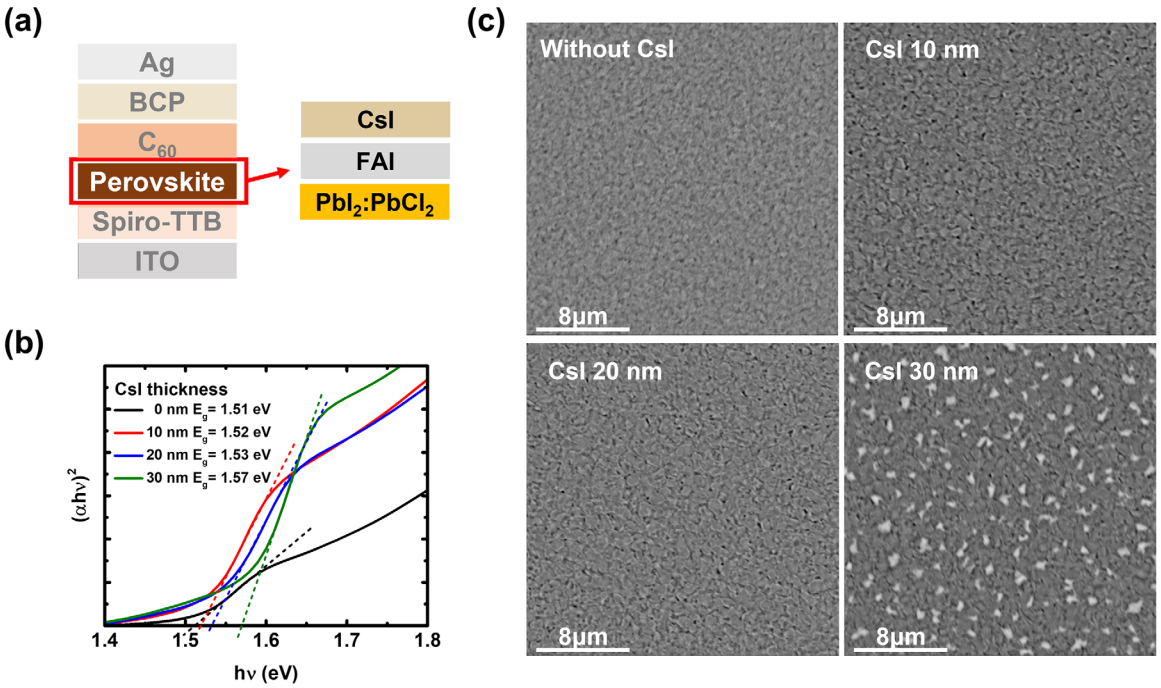

FIGURE 4 | (a) Device architecture and CsI-assisted sequential deposition process. (b) Tauc plots of perovskite films with varying CsI thicknesses. (c) Top-view SEM images of corresponding perovskite films.

needle-like crystals contain 21.08% nitrogen (N) and only 0.52% cesium (Cs). In comparison, the standard perovskite crystals exhibit a higher Cs content (2.11%) and a lower N ratio (16.81%), suggesting inconsistent incorporation of Cs into the perovskite lattice. These results indicate that excessive CsI thickness disrupts compositional uniformity and triggers phase separation within the perovskite film.

To evaluate the impact of CsI incorporation on fully evaporated PSCs, we employed TL84 fluorescent illumination as a standardized indoor light source representing typical commercial office environments. Ambient-light illuminance can be broadly classified into four categories: high-contrast tasks (750–1000 lx), reading tasks (420–750 lx), basic visual tasks (200–420 lx), and low-level illumination (<200 lx) [42]. Accordingly, three representative illumination intensities, 900, 600, and 300 lx, were selected for device evaluation. Figure 5a shows the emission spectrum of the TL84 light source, featuring characteristic peaks at 434, 544, and 612 nm. The corresponding power densities at 900, 600, and 300 lx are 263.63, 177.57, and 90.45 μW cm^{-2}, respectively. Importantly, no spectral shift is observed with varying illumination intensity, ensuring consistent spectral conditions for reliable performance comparison. Devices fabricated using perovskite layers with different CsI thicknesses were characterized under TL84 illumination, and the corresponding J-V curves and performance parameters are summarized in Table 1 and Figure 5b. For the pristine one, the fully evaporated PSC exhibits a PCE of 13.07%, an open-circuit voltage (V_{oc}) of 0.755 V, a short-circuit current density (J_{sc}) of 91.26 μA cm^{-2}, and a fill factor (FF) of 50.02% under 900 lx. Upon reducing the illumination intensity to 600 and 300 lx, the PCE decreases to 11.32% and 4.55%, respectively, primarily due to pronounced losses in V_{oc} and FF. In comparison, PSCs based on perovskite films incorporating 10 nm CsI exhibit substantially improved performance, achieving a PCE of 39.82% under 900 lx, with a V_{oc} of 0.776 V, a J_{sc} of 185.61 μA cm^{-2}, FF of 73.33%. When the illumination intensity decreases to 600 and 300 lx, the PCE remains relatively high at 30.07% and 24.07%, respectively. Further optimization is achieved with 20 nm CsI incorporation, yielding the highest PCE of 41.60% under 900 lx, along with a V_{oc} of 0.811 V, a J_{sc} of 180.77 μA cm^{-2}, FF of 75.85%. Notably, this device maintains remarkably stable efficiencies of 41.57% and 41.22% under 600 and 300 lx illumination, respectively. These results demonstrate that CsI-mediated defect passivation and phase stabilization significantly enhance the crystallinity and electronic quality of FA-based perovskite films, effectively suppressing defect-induced recombination under low-light conditions. Consequently, a CsI thickness of 20 nm is identified as the optimal condition for fully evaporated perovskite films tailored for ambient-light harvesting applications. Figure S5 presents the external quantum efficiency (EQE) spectra and the corresponding integrated J_{sc} for the optimized PSCs. Utilizing the TL84 900 lx spectrum (illustrated in Figure 5a), the EQE data was integrated to yield a calculated J_{sc} of 187.04 μA cm^{-2}. This result shows excellent consistency with the experimentally measured J_{sc} value of 180.77 μA cm^{-2} listed in Table 1.

To probe the effect of CsI incorporation on charge-carrier dynamics in fully evaporated PSCs, TPV and TPC measurements were performed. As shown in Figure 6a, TPV measurements under open-circuit conditions reveal that introducing 20 nm CsI prolongs the carrier lifetime from 3.45 to 4.21 ms, indicating suppressed nonradiative recombination [43, 44]. This enhancement is attributed to reduced lattice strain and effective defect passivation, which are particularly critical under low-intensity ambient illumination. TPC measurements further demonstrate improved charge extraction behavior. As summarized in Figure 6b and Table S1, the carrier extraction time decreases from 0.80 to 0.71 μs

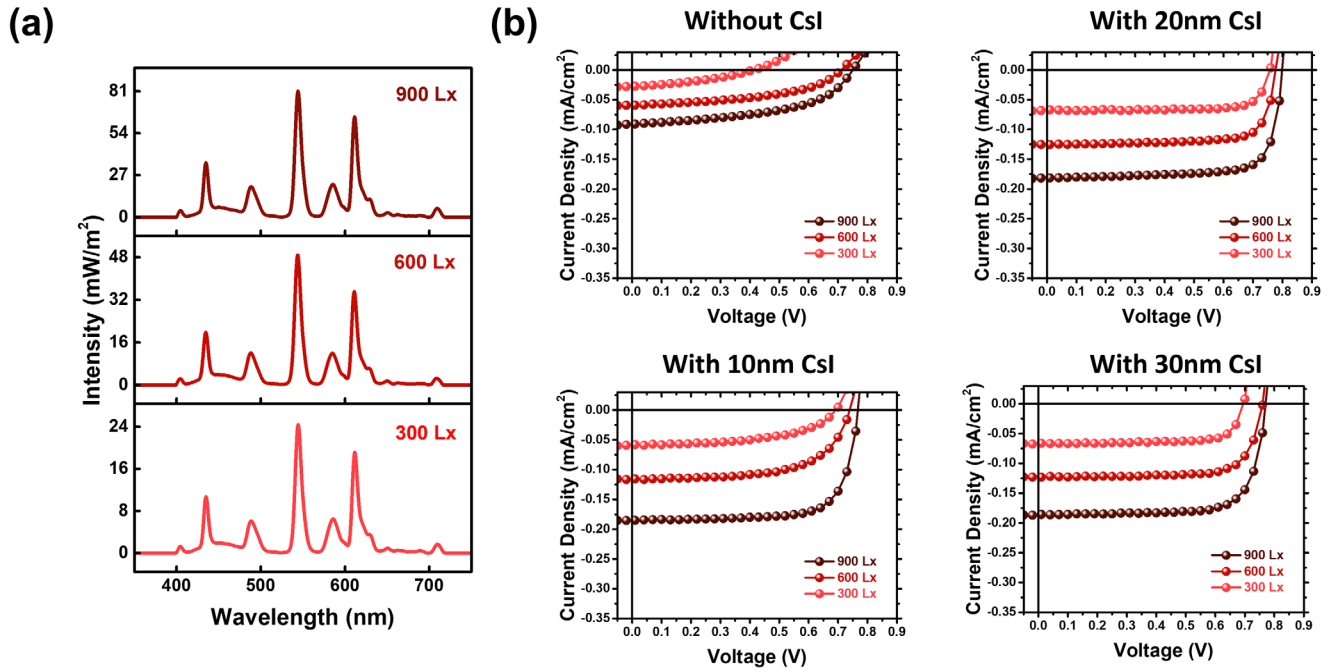

FIGURE 5 | (a) TL84 emission spectra at 900, 600, and 300 lx. (b) *J–V* curves of fully evaporated perovskite solar cells with varying CsI thicknesses measured under TL84 illumination.

TABLE 1 | Device performance of fully evaporated perovskite solar cells with varying CsI thicknesses measured under TL84 illumination.

Condition	Light intensity (lx)	Light intensity (μW cm^{-2})	V_{oc} (V)	J_{sc} (μA cm^{-2})	FF (%)	PCE (%)
Pristine	900	263.63	0.755	91.26	50.02	13.07
	600	177.57	0.713	59.41	47.45	11.32
	300	90.45	0.412	27.60	36.15	4.55
10 nm CsI	900	263.63	0.776	185.61	73.33	39.82
	600	177.57	0.746	115.43	61.99	30.07
	300	90.45	0.704	58.45	52.90	24.07
20 nm CsI	900	263.63	0.811	180.77	75.85	41.60
	600	177.57	0.802	125.60	74.82	41.57
	300	90.45	0.764	68.11	73.58	41.22
30 nm CsI	900	263.63	0.783	186.22	74.31	41.08
	600	177.57	0.761	122.95	74.77	39.40
	300	90.45	0.735	66.45	71.52	38.61

upon incorporation of 20 nm CsI layer, indicating more efficient charge extraction and suppressed deep-trap-assisted recombination. To further evaluate the reduction in non-radiative losses, we measured the photoluminescence quantum yield (PLQY) of the perovskite films and converted the results into quasi-Fermi level splitting (QFLS) values. QFLS serves as a quantitative metric that reflects the total non-radiative recombination losses originating from both the perovskite bulk and interfacial regions [45, 46]. As shown in Figure S6, the PLQY mapping of perovskite films with different structures reveals distinct differences in film quality. The control film prepared from pure PbI_2 exhibits a non-uniform PLQY distribution, indicating a high density of localized defects and inhomogeneous crystallization. In contrast, incorporating $PbCl_2$ significantly enhances PLQY and produces a more spatially uniform emission profile, suggesting reduced defect density and improved crystallization uniformity. This improvement is further quantified through QFLS analysis (Figure S7). The QFLS increases from 0.979 to 1.022 eV after introducing $PbCl_2$, indicating reduced non-radiative recombination losses. With the additional incorporation of CsI, the QFLS further increases to 1.044 eV. This enhancement can be attributed to the dual role of Cs^+ ions, which stabilize the perovskite lattice and

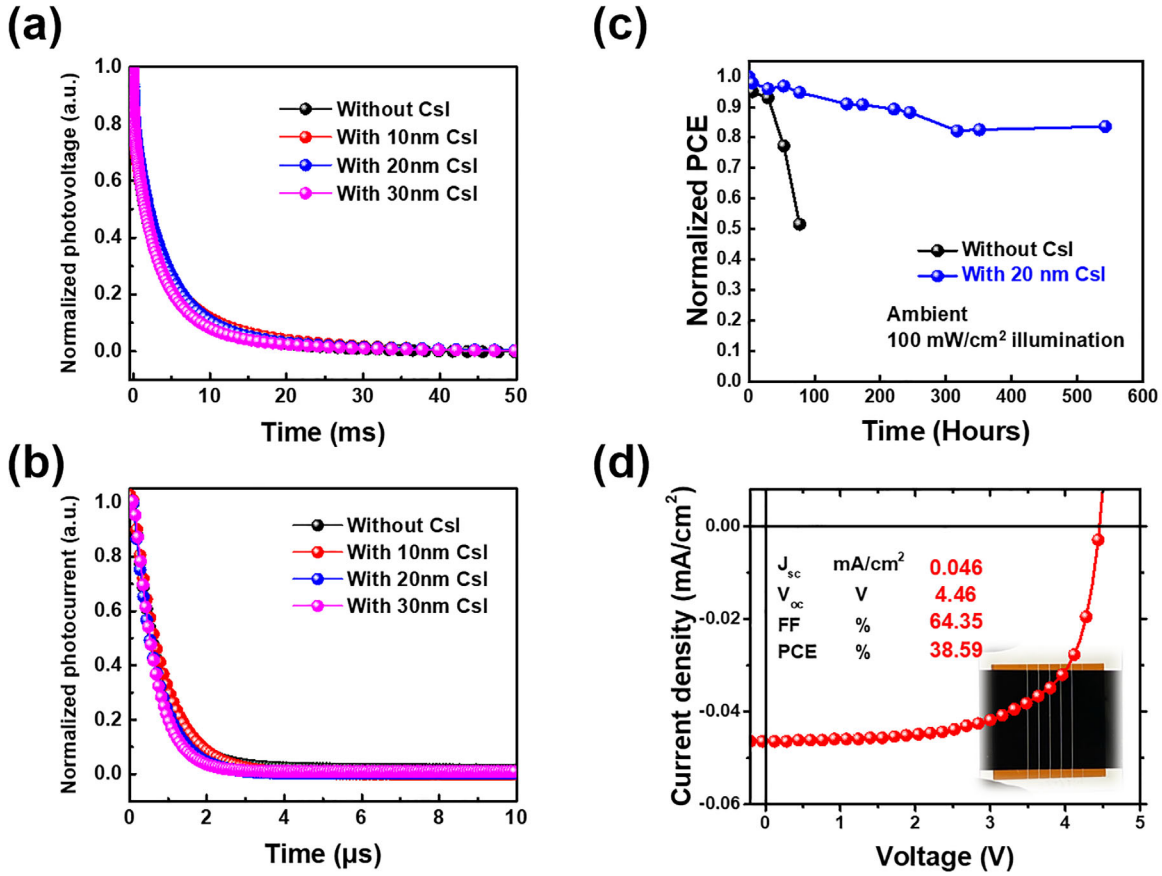

FIGURE 6 | (a) TPV and (b) TPC decay of fully evaporated perovskite solar cells with different CsI thicknesses. (c) Operational stability under ISOS-L-1 conditions. (d) *J–V* characteristics of a 3.9 cm^2 perovskite module measured under 900 lx TL84 illumination.

mitigate surface cation vacancies. Overall, these results demonstrate the complementary roles of $PbCl_2$ and CsI in suppressing non-radiative recombination by improving both bulk crystallinity and interfacial electronic quality. The strong light power also can accelerate the defect-induced degradation. Operational stability was evaluated under ISOS-L-1 conditions (100 mW cm^{-2}, 25°C, 55% relative humidity), as shown in Figure 6c [47]. Devices incorporating 20 nm CsI retain 83% of their initial efficiency after 543 h of continuous illumination, whereas control devices without CsI exhibit a T_{80} lifetime of only 53 h, highlighting the critical role of CsI-mediated defect management in enhancing long-term stability. Figures S8 and S9 illustrate the batch-to-batch reproducibility and thickness uniformity of the evaporated perovskite films, respectively. The high consistency observed across multiple fabrication cycles highlights the stability and scalability of the thermal evaporation process. Furthermore, a perovskite mini-module with an active area of 3.9 cm^2 achieves a power conversion efficiency exceeding 38% under 900 lx TL84 illumination, as shown in Figure 6d. These results represent, to the best of our knowledge, the highest reported performances for fully evaporated indoor PSCs to date.

3 | Conclusion

In conclusion, we establish a fully vacuum-processed perovskite photovoltaic platform specifically optimized for indoor energy harvesting. Through the synergistic integration of $PbCl_2$-assisted inorganic precursor engineering and CsI-mediated phase stabilization, uniform perovskite crystallization is achieved alongside suppressed defect formation and improved charge-carrier dynamics. This vacuum-evaporation strategy delivers state-of-the-art indoor power conversion efficiencies exceeding 41%, while simultaneously enabling enhanced operational stability and scalable mini-module fabrication. Collectively, this work presents a practical and industrially viable methodology for realizing high-performance, fully evaporated perovskite photovoltaics, advancing their deployment in self-powered indoor and Internet-of-Things applications.

4 | Experimental Procedure

4.1 | Materials

2,2′,7,7′-Tetra(N,N-di-p-tolyl)amino-9,9-spirobifluorene (Spiro-TTB, 99%) was obtained from Tetrahedron Technology. Perovskite Precursors and other components were sourced from several suppliers. Thermo Scientific Chemicals provided the inorganic precursors, including lead iodide (PbI_2, 99.9985% metal basis), lead chloride ($PbCl_2$, 99%), and cesium iodide (CsI, 99.999% metals basis). Formamidinium iodide (FAI, >99.99%) was purchased from Greatcell Solar. Fullerene (C_{60}) was supplied by 1-Material. 2,9-Dimethyl-4,7-diphenyl-1,10-phenanthroline (BCP) was purchased from Shine Materials. All chemicals were used as received without further purification.

4.2 | Device Fabrication for Perovskite Solar Cells

Indium-Tin oxide coated glass substrates (ITO, 15 Ω per sq, Luminescence Technology) were sequentially cleaned by ultrasonic treatment and then transferred into a thermal evaporation system (Syskey Technology). The chamber pressure below 1×10^{-6} torr was achieved prior to deposition. Spiro-TTB (3 nm) was first deposited as the hole-transporting layer at a rate of 0.2 Å s^{-1}. The inorganic perovskite precursor layer (175 nm) was then thermally evaporated at a PbI_2 deposition rate of 3 Å s^{-1}, with $PbCl_2$ co-evaporated at controlled rates as specified. Subsequently, a 200 nm FAI layer was deposited at 1 Å s^{-1}, followed by deposition of CsI with varying thicknesses at a rate of 0.5 Å s^{-1}. The as-deposited films were thermally annealed at 135°C for 30 min in ambient air to complete the perovskite phase conversion, during which the films turned dark brown. Electron-transport layers and electrodes were deposited sequentially by thermal evaporation, consisting of C_{60} (20 nm, 0.2 Å s^{-1})/BCP (7 nm, 0.2 Å s^{-1})/Ag (150 nm, 3 Å s^{-1}) multilayer structure. Film thicknesses were measured by using a profilometer (Bruker, DektakXT). The device active area was defined as 4 mm^2. The completed devices were encapsulated under an inert nitrogen-filled glovebox (O_2< 0.1 ppm; H_2O < 0.1 ppm) to preclude air ingress. The sealing process utilized a glass-to-glass encapsulation technique with EXC345 (Everwide Chemical Corporation), a UV-curable epoxy resin.

4.3 | Characterization

Photovoltaic performance under indoor illumination was evaluated using TL84 fluorescent light sources, with current–voltage (*I–V*) characteristics recorded using a source meter (Keithley 2410) integrated within a calibrated measurement system at the Industrial Technology Research Institute (ITRI). The system was designed with blackened internal walls to suppress reflections of stray light and ensure uniform illumination conditions. Prior to the *I–V* measurements, both the luminance and irradiance of the light source were carefully calibrated using a lux meter (TES, model 1332A) and a spectroradiometer (Optimum Optoelectronics Corp., SRI-2000). To ensure measurement accuracy, the sample height was fixed to align with the focal plane of the spectroradiometer, which was positioned at the center of the measurement system. During the measurements, the indoor illumination intensity was maintained at a constant lux level, while the corresponding irradiance was precisely adjusted to match the targeted calibration values. External quantum efficiency (EQE) spectra were obtained using a QE measurement system (Enlitech QE-R) operated in AC mode and calibrated with a silicon reference photodiode (Hamamatsu S1337). Photostability tests were performed under continuous illumination equivalent to AM 1.5G 1-sun intensity using a white LED source (LSH-7320, Newport). X-ray diffraction (XRD) patterns were recorded with a diffractometer (D2 PHASER, Bruker). Surface morphology was characterized using atomic force microscopy (AFM, Bruker Innova). Transient photovoltage (TPV) and transient photocurrent (TPC) measurements were conducted using an all-in-one system (Paios, Fluxim AG). Top-view and Cross-sectional morphologies were examined by field-emission scanning electron microscopy (FESEM, Hitachi SU8010). The characterization of photoluminescence quantum yield (PLQY) and quasi-Fermi level splitting (QFLS) was conducted by QFLS-Maper (Enli Technology Co., Ltd).

4.4 | Module Fabrication

Perovskite solar modules were fabricated on 4 cm × 4 cm fluorine-doped tin oxide (FTO) glass substrates. The module design consisted of five sub-cells connected in series through P1–P2–P3 laser interconnections. Initially, the FTO layer was patterned using a 532 nm laser to define the P1 lines, with a spacing of 0.3 cm between adjacent lines. After deposition of the functional layers, P2 lines were formed by laser scribing to expose the underlying FTO. A 150 nm Ag electrode was then thermally evaporated, followed by laser scribing of the P3 lines. The distance between the P1 and P3 lines was approximately 200 μm, resulting in a geometric factor (GFF) of 94%.

Author Contributions

Shih-Han Huang: methodology, investigation, formal analysis, validation, data curation, writing – original draft, visualization. **Ssu-Yung Chung**: investigation, formal analysis, validation, data curation. **Fang-Chun Su**: investigation, formal analysis. **Chia-Feng Li**: data curation, visualization. **You-Ren Chen**: investigation, data curation. **Ting-Han Lin**: investigation, data curation. **Hou-Chin Cha**: visualization, data curation, funding acquisition. **Yi-Sheng Chen**: methodology. **Chih-Chien Lee**: resources. **Yu-Ching Huang**: conceptualization, methodology, resources, writing – review & editing, supervision, project administration, funding acquisition. **Shun-Wei Liu**: conceptualization, methodology, resources, writing – review & editing, supervision, project administration, funding acquisition.

Acknowledgements

The authors sincerely thank the National Science and Technology Council for their generous financial support (Grant Nos. NSTC-113-2221-E-131-021-MY3, 113-2622-E-131-009, 114-2221-E-131-005-MY2, 114-2622-E-131-006, 114-2222-E-131-004, 112-2628-E-131-001-MY4, 114-2622-E-131-007, 114-2221-E-131-012-MY3, 114-2222-E-131-002). The corresponding author, S.-W. Liu, profoundly appreciates the invaluable contributions of Mr. Hsueh-Hsien Wu from Syskey Technology Co., Ltd. (Taiwan) in the design of the fabrication chambers, which played a critical role in advancing this work. The authors also gratefully acknowledge the financial support provided by Chang Gung University (Grant No. URRPD2N0011) and Ming Chi University of Technology's Formosa Center (Grant No. FM002-113), which were pivotal to the successful completion of this research.

Conflicts of Interest

The authors declare no conflicts of interest.

Data Availability Statement

The data that support the findings of this study are available from the corresponding author upon reasonable request.

References

1. J. Gubbi, R. Buyya, S. Marusic, and M. Palaniswami, "Internet of Things (IoT): A Vision, Architectural Elements, and Future Directions," *Future Generation Computer Systems* 29 (2013): 1645–1660, https://doi.org/10.1016/j.future.2013.01.010.

2. T. Sanislav, G. D. Mois, S. Zeadally, and S. C. Folea, "Energy Harvesting Techniques for Internet of Things (IoT)," *IEEE Access* 9 (2021): 39530–39549, https://doi.org/10.1109/ACCESS.2021.3064066.

3. J. Hester and J. Sorber, in *Proceedings of the 15th ACM Conference on Embedded Network Sensor Systems* (Association for Computing Machinery, 2017), 19.

4. Y. Chen, Y. Kang, Y. Zhao, et al., "A Review of Lithium-Ion Battery Safety Concerns: The Issues, Strategies, and Testing Standards," *Journal of Energy Chemistry* 59 (2021): 83–99, https://doi.org/10.1016/j.jechem.2020.10.017.

5. R. Haight, W. Haensch, and D. Friedman, "Solar-powering the Internet of Things," *Science* 353 (2016): 124–125, https://doi.org/10.1126/science.aag0476.

6. H. Michaels, I. Benesperi, and M. Freitag, "Challenges and Prospects of Ambient Hybrid Solar Cell Applications," *Chemical Science* 12 (2021): 5002–5015.

7. K. Yoshikawa, H. Kawasaki, W. Yoshida, et al., "Silicon Heterojunction Solar Cell With Interdigitated Back Contacts for a Photoconversion Efficiency Over 26%," *Nature Energy* 2 (2017): 17032, https://doi.org/10.1038/nenergy.2017.32.

8. E. Cuce, P. M. Cuce, and T. Bali, "An Experimental Analysis of Illumination Intensity and Temperature Dependency of Photovoltaic Cell Parameters," *Applied Energy* 111 (2013): 374–382, https://doi.org/10.1016/j.apenergy.2013.05.025.

9. H. Águas, T. Mateus, A. Vicente, et al., "Thin Film Silicon Photovoltaic Cells on Paper for Flexible Indoor Applications," *Advanced Functional Materials* 25 (2015): 3592–3598, https://doi.org/10.1002/adfm.201500636.

10. M.-J. Wu, C.-C. Kuo, L.-S. Jhuang, P.-H. Chen, Y.-F. Lai, and F.-C. Chen, "Bandgap Engineering Enhances the Performance of Mixed-Cation Perovskite Materials for Indoor Photovoltaic Applications," *Advanced Energy Materials* 9 (2019): 1901863, https://doi.org/10.1002/aenm.201901863.

11. B. Hou, B.-S. Kim, H. K. H. Lee, et al., "Multiphoton Absorption Stimulated Metal Chalcogenide Quantum Dot Solar Cells Under Ambient and Concentrated Irradiance," *Advanced Functional Materials* 30 (2020): 2004563, https://doi.org/10.1002/adfm.202004563.

12. W. Wang, Y. Cui, T. Zhang, et al., "High-Performance Organic Photovoltaic Cells Under Indoor Lighting Enabled by Suppressing Energetic Disorders," *Joule* 7 (2023): 1067–1079, https://doi.org/10.1016/j.joule.2023.04.003.

13. C.-C. Chen, V. S. Nguyen, H.-C. Chiu, Y.-D. Chen, T.-C. Wei, and C.-Y. Yeh, "Anthracene-Bridged Sensitizers for Dye-Sensitized Solar Cells With 37% Efficiency Under Dim Light," *Advanced Energy Materials* 12 (2022): 2104051, https://doi.org/10.1002/aenm.202104051.

14. Q. Ma, Y. Wang, L. Liu, et al., "One-Step Dual-Additive Passivated Wide-Bandgap Perovskites to Realize 44.72%-Efficient Indoor Photovoltaics," *Energy & Environmental Science* 17 (2024): 1637–1644, https://doi.org/10.1039/D3EE04022D.

15. T. Abzieher, D. T. Moore, M. Roß, et al., "Vapor Phase Deposition Of Perovskite Photovoltaics: Short Track to Commercialization?," *Energy & Environmental Science* 17 (2024): 1645–1663, https://doi.org/10.1039/D3EE03273F.

16. F. U. Kosasih, E. Erdenebileg, N. Mathews, S. G. Mhaisalkar, and A. Bruno, "Thermal Evaporation and Hybrid Deposition of Perovskite Solar Cells and Mini-Modules," *Joule* 6 (2022): 2692–2734, https://doi.org/10.1016/j.joule.2022.11.004.

17. J. Li, R. Gao, F. Gao, et al., "Fabrication of Efficient $CsPbBr_3$ Perovskite Solar Cells by Single-Source Thermal Evaporation," *Journal of Alloys and Compounds* 818 (2020): 152903, https://doi.org/10.1016/j.jallcom.2019.152903.

18. M. Chen, M.-G. Ju, H. F. Garces, et al., "Highly Stable and Efficient All-Inorganic Lead-Free Perovskite Solar Cells With Native-Oxide Passivation," *Nature Communications* 10 (2019): 16, https://doi.org/10.1038/s41467-018-07951-y.

19. S. Kralj, K. Artuk, A. Wieczorek, et al., "Template-Assisted Growth of $Cs_xFA_{1-x}PbI_3$ With Pulsed Laser Deposition for Single Junction Perovskite Solar Cells," *Advanced Energy Materials* 15 (2025): 2406033, https://doi.org/10.1002/aenm.202406033.

20. C.-W. Chen, H.-W. Kang, S.-Y. Hsiao, P.-F. Yang, K.-M. Chiang, and H.-W. Lin, "Efficient and Uniform Planar-Type Perovskite Solar Cells by Simple Sequential Vacuum Deposition," *Advanced Materials* 26 (2014): 6647–6652, https://doi.org/10.1002/adma.201402461.

21. J. Feng, Y. Jiao, H. Wang, et al., "High-Throughput Large-Area Vacuum Deposition For High-Performance Formamidine-Based Perovskite Solar Cells," *Energy & Environmental Science* 14 (2021): 3035–3043, https://doi.org/10.1039/D1EE00634G.

22. Y. Xu, K. Xu, T. Pan, et al., "Fully Thermally Evaporated Perovskite Solar Cells Based On Reverse Layer-By-Layer Deposition," *Nature Photonics* 19 (2025): 1345–1352, https://doi.org/10.1038/s41566-025-01768-0.

23. Q. Lin, A. Armin, R. C. R. Nagiri, P. L. Burn, and P. Meredith, "Electro-Optics of Perovskite Solar Cells," *Nature Photonics* 9 (2015): 106–112, https://doi.org/10.1038/nphoton.2014.284.

24. N. R. Al Amin, C.-C. Lee, Y.-C. Huang, et al., "Achieving a Highly Stable Perovskite Photodetector With a Long Lifetime Fabricated via an All-Vacuum Deposition Process," *ACS Applied Materials & Interfaces* 15 (2023): 21284–21295, https://doi.org/10.1021/acsami.3c00839.

25. Y. Liu, J. Yang, Q. Luo, et al., "Vacuum Co-Evaporated Wide-Bandgap Perovskite Films For Highly-Efficient Indoor Photovoltaic Cells And Modules," *Surfaces and Interfaces* 36 (2023): 102648, https://doi.org/10.1016/j.surfin.2023.102648.

26. Q. Ma, M. Ma, L. Liu, et al., "Wide-Band-Gap Perovskite Solar Minimodules Exceeding 43% Efficiency Under Indoor Light Illumination," *Device* 1 (2023): 100174, https://doi.org/10.1016/j.device.2023.100174.

27. X. He, J. Chen, X. Ren, et al., "40.1% Record Low-Light Solar-Cell Efficiency by Holistic Trap-Passivation using Micrometer-Thick Perovskite Film," *Advanced Materials* 33 (2021): 2100770, https://doi.org/10.1002/adma.202100770.

28. C. Zhang, C. Liu, Y. Gao, et al., "Br Vacancy Defects Healed Perovskite Indoor Photovoltaic Modules With Certified Power Conversion Efficiency Exceeding 36%," *Advanced Science* 9 (2022): 2204138, https://doi.org/10.1002/advs.202204138.

29. T. Du, W. Xu, S. Xu, et al., "Light-Intensity and Thickness Dependent Efficiency of Planar Perovskite Solar Cells: Charge Recombination Versus Extraction," *Journal of Materials Chemistry C* 8 (2020): 12648–12655, https://doi.org/10.1039/D0TC03390A.

30. Y.-C. Huang and C.-F. Li, "Insights Into the Photovoltaic Mechanism of Organic Photovoltaics Under Solar and Artificial Light," *Journal of Materials Chemistry C* 11 (2023): 14079–14087, https://doi.org/10.1039/D3TC02372A.

31. C.-F. Li, S.-H. Cheng, H.-C. Cha, et al., "Tailoring the Transport Layer Interface for Relative Indoor and Outdoor Photovoltaic Performance," *ACS Applied Energy Materials* 7 (2024): 10203–10211, https://doi.org/10.1021/acsaem.4c02521.

32. C.-H. Chen, Z.-H. Su, Y.-H. Lou, et al., "Full-Dimensional Grain Boundary Stress Release for Flexible Perovskite Indoor Photovoltaics," *Advanced Materials* 34 (2022): 2200320, https://doi.org/10.1002/adma.202200320.

33. H. Li, J. Zhou, L. Tan, et al., "Sequential Vacuum-Evaporated Perovskite Solar Cells With More Than 24% efficiency," *Science Advances* 8 (2022): abo7422, https://doi.org/10.1126/sciadv.abo7422.

34. L. Tan, J. Zhou, X. Zhao, et al., "Combined Vacuum Evaporation and Solution Process for High-Efficiency Large-Area Perovskite Solar Cells With Exceptional Reproducibility," *Advanced Materials* 35 (2023): 2205027, https://doi.org/10.1002/adma.202205027.

35. Q. Luo, M. Wu, H. Zhang, et al., "Combined Evaporation-Solution Methodology For High-Efficiency Perovskite Solar Cells With Exceptional Reproducibility," *Journal of Materials Chemistry A* 13 (2025): 25782–25789, https://doi.org/10.1039/D5TA03304G.

36. S. T. Williams, F. Zuo, C.-C. Chueh, C.-Y. Liao, P.-W. Liang, and A. K. Y. Jen, "Role of Chloride in the Morphological Evolution of Organo-Lead Halide Perovskite Thin Films," *ACS Nano* 8 (2014): 10640–10654, https://doi.org/10.1021/nn5041922.

37. A. Greco, A. Hinderhofer, M. I. Dar, et al., "Kinetics of Ion-Exchange Reactions in Hybrid Organic–Inorganic Perovskite Thin Films Studied by In Situ Real-Time X-ray Scattering," *Journal of Physical Chemistry Letters* 9 (2018): 6750–6754, https://doi.org/10.1021/acs.jpclett.8b02916.

38. S.-H. Huang, K.-Y. Tian, H.-C. Huang, et al., "Controlling the Morphology and Interface of the Perovskite Layer for Scalable High-Efficiency Solar Cells Fabricated Using Green Solvents and Blade Coating in an Ambient Environment," *ACS Applied Materials & Interfaces* 12 (2020): 26041–26049, https://doi.org/10.1021/acsami.0c06211.

39. Z. Li, J. Zhang, S. Wu, et al., "Minimized Surface Deficiency on Wide-Bandgap Perovskite for Efficient Indoor Photovoltaics," *Nano Energy* 78 (2020): 105377, https://doi.org/10.1016/j.nanoen.2020.105377.

40. M. Wang, Q. Wang, J. Zhao, et al., "Low-Trap-Density $CsPbX_3$ Film for High-Efficiency Indoor Photovoltaics," *ACS Applied Materials & Interfaces* 14 (2022): 11528–11537, https://doi.org/10.1021/acsami.1c25207.

41. M. H. Ann, J. Kim, M. Kim, et al., "Device Design Rules and Operation Principles of High-Power Perovskite Solar Cells for Indoor Applications," *Nano Energy* 68 (2020): 104321, https://doi.org/10.1016/j.nanoen.2019.104321.

42. J. K. W. Ho, H. Yin, and S. K. So, "From 33% to 57%—an Elevated Potential of Efficiency Limit for Indoor Photovoltaics," *Journal of Materials Chemistry A* 8 (2020): 1717–1723, https://doi.org/10.1039/C9TA11894B.

43. D. Kiermasch, A. Baumann, M. Fischer, V. Dyakonov, and K. Tvingstedt, "Revisiting Lifetimes From Transient Electrical Characterization Of Thin Film Solar Cells; A Capacitive Concern Evaluated for Silicon, Organic and Perovskite Devices," *Energy & Environmental Science* 11 (2018): 629–640, https://doi.org/10.1039/C7EE03155F.

44. Z. S. Wang, F. Ebadi, B. Carlsen, W. C. H. Choy, and W. Tress, "Transient Photovoltage Measurements on Perovskite Solar Cells With Varied Defect Concentrations and Inhomogeneous Recombination Rates," *Small Methods* 4 (2020): 2000290, https://doi.org/10.1002/smtd.202000290.

45. G. Seo, J. J. Yoo, S. Nam, et al., "Efficient and Luminescent Perovskite Solar Cells Using Defect-Suppressed SnO_2 via Excess Ligand Strategy," *Nature Energy* 10 (2025): 774–784, https://doi.org/10.1038/s41560-025-01781-1.

46. X. Yang, K. Jing, H. Zhang, et al., "Unveiling the Myths of Co-Deposition of Hole Conductors and Perovskite Layers," *Small* 22 (2026): 13227, https://doi.org/10.1002/smll.202513227.

47. M. V. Khenkin, E. A. Katz, A. Abate, et al., "Consensus Statement for Stability Assessment and Reporting for Perovskite Photovoltaics Based on ISOS Procedures," *Nature Energy* 5 (2020): 35–49.

Supporting Information

Additional supporting information can be found online in the Supporting Information section.

Supporting File: smtd70654-sup-0001-SuppMat.pdf.